Step-bunching instability of growing interfaces between ice and supercooled water

Ken-ichiro Murata[a,1], Masahide Sato[b], Makio Uwaha[c], Fumiaki Saito[a], Ken Nagashima[a], and Gen Sazaki[a]

[a]Institute of Low Temperature Science, Hokkaido University, Kita-ku, Sapporo 060-0819, Japan; [b]Emerging Media Initiative, Kanazawa University, Kakuma-machi, Kanazawa 920-1192, Japan; and [c]Center for General Education, Aichi Institute of Technology, Yakusa-cho, Toyota 470-0392, Japan

Ice-crystal growth in supercooled water is one of the most familiar examples of phase-transition dynamics, playing essential roles in various natural phenomena on Earth. Despite its fundamental importance, the microscopic view at the elementary step level remains elusive. Here, using an advanced optical microscope, we find self-organization of elementary steps during ice-crystal growth, called step-bunching instability (SBI), driven by the competition between step dynamics, interfacial stiffness, and latent heat diffusions. We also find that the SBI transiently induces screw dislocations and resulting spiral growth in the late stage of the growth process. Furthermore, quantitative observations with a two-beam interferometer allow us to obtain insights into the relative importance of the various mechanisms of the step–step interactions. Our finding offers a significant clue to understanding the general mechanism of melt growth beyond ice-crystal growth, inseparably involving several broad research fields, including cryobiological, geophysical, and material branches.

Step-bunching instability | ice-crystal growth | melt growth | in situ observation | screw dislocation

Crystallization of a material from its own supercooled melt is one of the most fundamental phase transitions, governing the state of matter. Ice crystallization from supercooled water is the most familiar example, not only seen in our everyday life, such as when making ice in freezers, food processing, and preservation, but also playing an essential role in a diverse set of natural phenomena on Earth, such as cloud formation, frost heave, ice accretion, and so forth (1–3). Due to its ubiquitous nature, in addition to ambient experimental conditions that are easy to access, ice-crystal growth in supercooled water has been a matter of intensive study for many years (Chapter 9 in ref. 4).

In general, the growth of crystals after initial nucleation proceeds through the kinetics of the interface, where incorporation of atoms and molecules takes place (5). The kinetics is known to be inseparably connected to the interfacial structure: the presence or absence of elementary steps (faceted or rough), dislocations, impurities, and so on (6). Despite its significant role, the microscopic to mesoscopic view of the interface between crystal (solid) and its melt (liquid) and its intrinsic link to the crystal growth are still far from completely understood. For ice growth in supercooled water (the so-called melt growth of ice), for example, Ketcham and Hobbs (7) directly observed macrosteps associated with spiral growth at an ice–water interface with optical microscopy. On the other hand, Furukawa and colleagues (8, 9) have intensively studied ice-crystal growth freely grown in supercooled water in microgravity, but observed no sign of such steps, even using more sophisticated optical microscopic techniques, phase-contrast microscopy combined with two-beam interferometry. The gap between their observations suggests a lack of fundamental information on the intrinsic nature of not only the ice–water interface, but also crystal–melt interfaces in general. Unfortunately, however, not much attention has been paid to this gap to date, and its origin remains elusive.

In this article, we shed light on the gap between their observations, using an advanced optical microscope. We demonstrate that the formation of macrosteps arises from self-organization of elementary steps, the so-called step-bunching instability (SBI) on vicinal faces of ice crystals. The SBI is a kind of interfacial instability: an instability of the equal-spacing step propagation on growing vicinal faces. So far, the SBI itself has been observed in a broad range of crystalline materials, such as semiconductors (10–16), inorganic crystals (17–20), and a protein crystal (21). It is also acknowledged that SBIs occur through various mechanisms, such as asymmetric step kinetics (22), repulsive step interactions (20, 23, 24), direct electric current (electromigration) (12, 14, 25–28), shear flow (19, 21, 29, 30), and impurities (10, 18, 31–33). However, for simple melt growth, there has been no firm experimental proof of the SBI so far, despite theoretical suggestions of its presence (34, 35). The lack of proof mainly comes from experimental difficulties of direct observations of growing interfaces in the melt at the step level. For example, although modern probe-based techniques, such as atomic force microscopy (AFM), are a promising candidate for observing surfaces and interfaces with high spatial and height resolutions, its application in an in situ manner is hampered by the extremely high growth rate of crystal–melt interfaces. Our optical microscopic approach, characterized by noncontact, noninvasion, and a wide field of view, has marked superiority in in situ observations of this system.

Here, we report convincing evidence of the SBI in pure melt growth and subsequent formations of screw dislocations and resulting spiral growth, taking ice-crystal growth as an example.

Significance

Step-bunching instability (SBI) is one of the interfacial instabilities driven by self-organization of elementary step flow associated with crystal-growth dynamics, which has been observed in diverse crystalline materials. However, despite theoretical suggestions of its presence, no direct observations of SBI for simple melt growth have been achieved so far. Here, with the aid of a type of optical microscope and its combination with a two-beam interferometer, we realized quantitative in situ observations of the spatiotemporal dynamics of the SBI. This enables us to examine the origin of the SBI at the level of the step–step interaction. We also found that the SBI spontaneously induces a highly stable spiral growth mode, governing the late stage of the growth process.
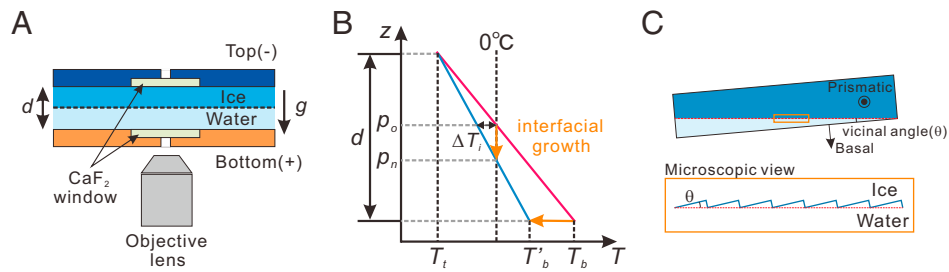
Fig. 1. The in situ observation system for ice–water interfaces. (*A*) A schematic of our observation system. The down black arrow labeled with g indicates the gravity direction, and d is the spacing between the top and the bottom plates ($d = 2{,}000\ \mu m$ in this study). (*B*) A schematic diagram of the relationship between a temperature gradient and an interfacial position in our system. Here, T_t and T_b indicate the temperature of the top plate and that of the bottom plate (see *A*), and p_o and p_n indicate the equilibrium position of the interface before and after changing the bottom temperature (from T_b to T'_b), respectively. ΔT_i is a maximum supercooling, $T - T_m$, at an interface. Note that we only changed T_b (T_t was fixed) in our observations. (*C*) A schematic of a vicinal face of an ice crystal realized in our experimental system. Here, θ corresponds to a vicinal angle against the genuine basal face. Microscopically, as shown in the orange rectangle, the initial vicinal face is composed of trains of elementary steps.

With the aid of optical microscopic techniques with ultrahigh height resolutions, we made direct visualizations of spatiotemporal dynamics of the SBI during the growth of ice and the spontaneous formation of the spiral growth induced by the SBI. In addition, using a two-beam interferometer, we directly measured not only the characteristic step spacing and the step-advancing velocity, but also the height of the bunched steps. This quantitative in situ approach allows us to elucidate the underlying mechanism of this SBI at the level of interactions between elementary steps.

We emphasize that dynamic modulation of the interface and defect formation dictated by the SBI hold a key to controlling the quality of crystals to be formed, which is crucial for material and industrial sciences. Furthermore, the SBI itself is intrinsically related to the inhibition of crystal growth. Thus, its understanding is also useful for applications to cryoprotection and cryopreservation of biological materials undamaged by ice crystallization (36). Our finding not only offers insights into crystal growth dynamics from the melt at a microscopic to mesoscopic level, but also has a significant impact on a wide range of research fields and applications, including geophysical, material, and cryobiological sciences.

Results and Discussion

In Situ Observation System for Ice–Water Interfaces. It is well known that the growth rate of crystals freely grown in melts is extremely fast compared to that of solution growth and vapor growth. For example, for ice-melt growth, the normal growth rate (normal to the facet) reaches 10^{-2} to 10^{-7} m/s (9), even for very weak supercooling. This high growth rate hampers direct and precise observations of growing interfaces, especially for those normal to the optical axis of the microscopy (a top view of crystal facets). In this study, to realize a moderate growth rate suitable for in situ optical observations of such interfaces, we developed a temperature gradient chamber. Fig. 1*A* shows a schematic of our observation system. Here, we set the upper temperature (T_t) below the ice-melting point and the lower (T_b) above the melting point, taking the density difference between ice and water into account. Due to the temperature gradient crossing the melting point, ice and water domains are initially divided by the 0 °C interface. In our observations, we changed the bottom temperature while keeping the top constant. As shown in Fig. 1*B*, when decreasing the bottom temperature, an ice domain starts to grow from p_o, and its growth front moves until arriving a new equilibrium position (p_n). This system makes the movement of the interface slow enough to follow with optical microscopy in an in situ manner and allows us to control the growth direction, normal to the interface (the so-called unidirectional solidification). We also note that, unlike the

free growth system, ice interfaces prepared by this chamber are not genuine basal faces, but have a finite vicinal angle θ (Fig. 1*C* and following discussions).

Furthermore, we employ advanced optical microscopy for in situ observations of growing interfaces, instead of laser confocal microscopy combined with differential interference microscopy (LCM-DIM) that we have conventionally employed (37–41). As shown in *SI Appendix* and *SI Appendix*, Fig. S1, in this microscopy, we simply replaced the Nomarski prism with an optical vortex retarder, while keeping the laser confocal unit unchanged. The height resolution of this microscopy reaches the subnanometer level, which is as high as that of LCM-DIM and AFM. We note that this microscopy has an advantage that an adjustment of the contrast is not necessary during the adjustment of a focal position of growing interfaces. For LCM-DIM, in contrast, to optimize the differential interference contrast (42) during the growth, we must adjust not only the focal position, but also the Nomarski prism at the same time, which is very difficult. Therefore, in this system, the optical microscopy is more suitable than LCM-DIM, although the height resolution is basically the same for each (*SI Appendix* and *SI Appendix*, Fig. S2).

Spatiotemporal Dynamics of SBI. Fig. 2 shows a typical example of a temporal process of an SBI on ice interfaces. Here, we changed T_b from 3.0 °C to 2.5 °C while fixing $T_t = -2.0$ °C. Note that, in our system, ice–water interfaces are composed of several single ice-crystal domains (the so-called polycrystalline state). During the SBI, we find the following three characteristic stages in the process. In the early stage, trains of bunched steps unidirectionally align on every single ice domain (Fig. 2*B*). In the intermediate stage, the formation and annihilation of the spiral growth modes occur intermittently. In the late stage, a single or a couple of spiral patterns are birthed by overlapping step flows from the surroundings and finally overwhelm every single ice-crystal interface (Fig. 2*C*). Hereafter, we will first focus on the SBI itself. Later, we will discuss origin of the spiral growth induced by the SBI.

Fig. 3*A* shows spatiotemporal dynamics of an SBI under a condition of $T_b = 2.5$ °C → 2.2 °C ($T_t = -2.0$ °C) (see also Movie S1). In the initial stage, bunched steps appear, which keep their spacing constant with accompanying meandering, terminations, and bifurcations (Fig. 3 *B* and *C*). In addition, the contrast of the steps, corresponding to their height, also immediately becomes constant. Here, note that the termination and bifurcation are not topological violations because the bunched steps can split up (disbanding or debunching). In Fig. 3*D*, we show the temporal change of the number of the terminations, the bifurcations, and its summation during the SBI (see also Movie S2). We find that, in the intermediate stage, the number of these "step defects"
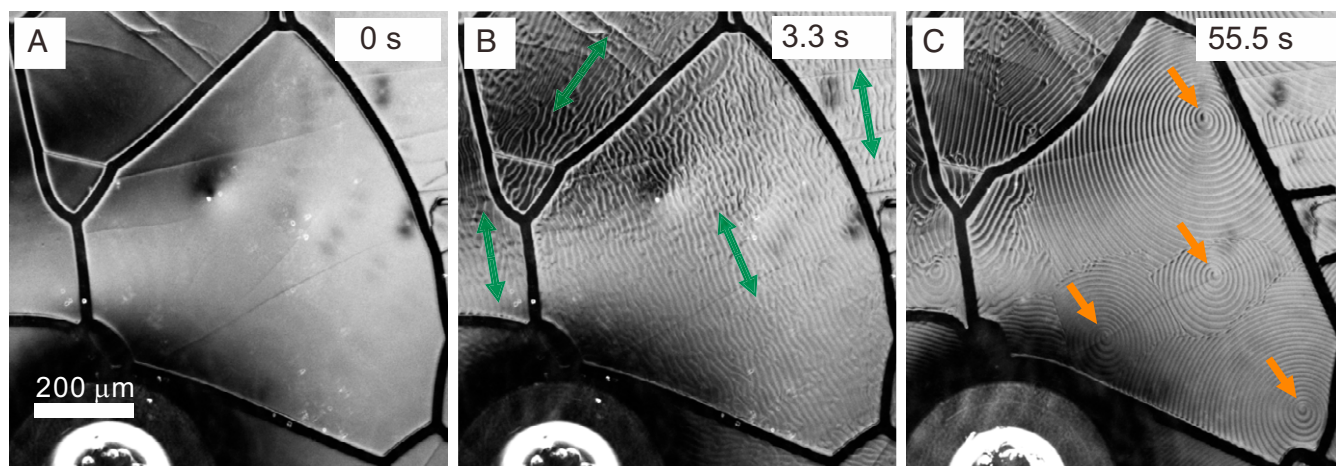
Murata et al.
Step-bunching instability of growing interfaces between ice
and supercooled water

Fig. 2. An SBI of a polycrystalline ice–water interface. (*A*) An ice-crystal interface before the SBI ($T_b = 3.0\,^\circ$C and $T_t = -2.0\,^\circ$C). (*B*) An initial stage of the SBI ($T_b = 3.0\,^\circ$C $\rightarrow$ 2.5 $^\circ$C and $T_t = -2.0\,^\circ$C). The green arrows show the directions along the bunched steps on each single ice crystal. (*C*) The late stage of the SBI. The orange arrows indicate the spiral centers intermittently induced by the SBI ($T_b = 2.5\,^\circ$C and $T_t = -2.0\,^\circ$C). (Scale bar; 200 μm.)

suddenly decreases around $t = 70$ s. As discussed below, this suggests that the growth mode shifts to spiral due to its formation outside of the observation area (see discussion below). Finally, in the late stage, as approaching a new equilibrium position of the interface, the bunched steps gradually disappear, while keeping their spacing constant.

Fig. 3*E* shows the temporal change in the step spacing l_{st} of the bunched steps during the SBI. It is worth noting that l_{st} keeps almost constant during the whole process (the mean value of l_{st} is 19.4 μm; see also Fig. 3*F*), not only after the initial stage, but also after the spiral formation. This means that there is no coarsening of the bunched steps in this system, which is distinct from other systems, exhibiting coarsening of steps (14, 26, 27, 43, 44). In these systems, coarsening of the step spacing is seen after the initial linear regime—that is, during the subsequent nonlinear

regime. In addition, Fig. 3*G* shows the temporal change of step velocity, v_{st}. We find that v_{st} gently increases from the initial stage and gradually decreases as the interface approaches to the new equilibrium position. Note that the mean value of v_{st} is estimated as 11.5 μm/s.

Next, we directly measured the height of bunched steps, using a two-beam interferometer combined with this microscopy. In addition to the step spacing and velocity, the step height is also an important quantity characterizing this instability. Fig. 4 *A* and *B* show interferometric images of an initial and a growing interface associated with the SBI, respectively. We see the shift of the interference fringes across the bunched steps (Fig. 4 *C* and *D*). The amount of the shift (ΔL) directly corresponds to their heights, h, of which relation is written by $h = \lambda \Delta L / 2nL$, where n is the refractive index of medium [$n = 1.334$, for water
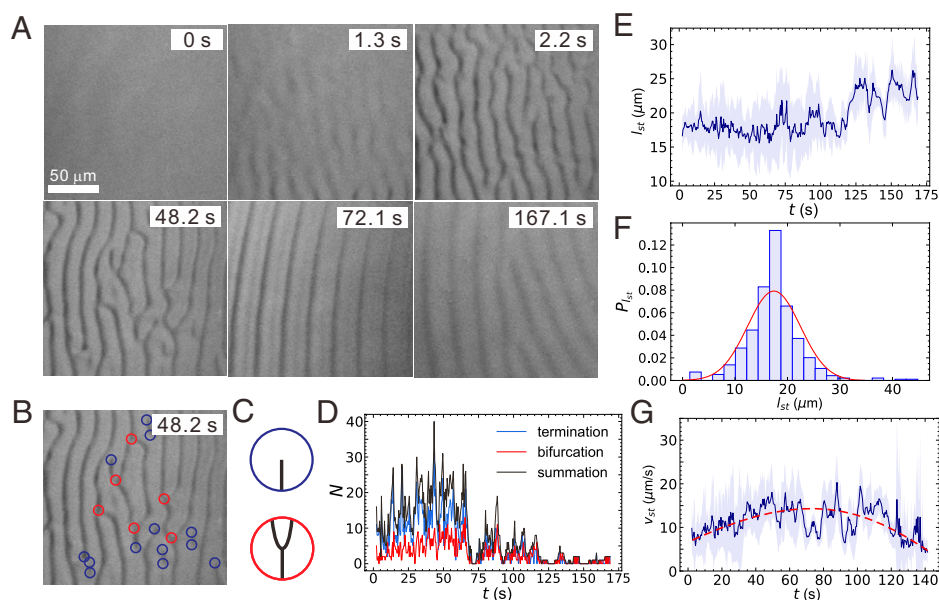
Fig. 3. Spatiotemporal dynamics of an SBI and its quantitative characterization. (*A*) Sequential images of pattern evolution of the SBI ($T_b = 2.5\,^\circ$C $\rightarrow$ 2.2 $^\circ$C and $T_t = -2.0\,^\circ$C). (Scale bar: 50 μm [see also Movie S1]). (*B*) A typical example of terminations (blue circles) and bifurcations (red circles) of bunched steps appearing in the SBI process (see also Movie S2). (*C*) A schematic of the termination (*Upper*) and the bifurcation (*Lower*) of the step. (*D*) A temporal change of the number of the step defects: the terminations (the blue line) and the bifurcations (the red line) and the summation of these two (the black line), respectively. (*E*) A temporal change of the spacing of the bunched step, l_{st}, during the SBI in A. (*F*) A histogram of the step spacing at $t = 39.3$ s as an example. (*G*) A temporal change of the advancing velocity of the bunched step, v_{st}, during the SBI in A. The red dashed line is a guide for the eye.

Murata et al.
Step-bunching instability of growing interfaces between ice and supercooled water

PNAS | 3 of 8
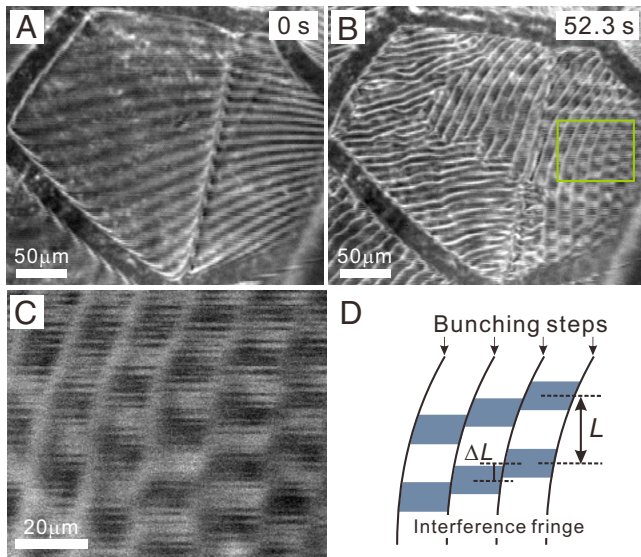https://doi.org/10.1073/pnas.2115955119

Fig. 4. Interferometric images of an ice–water interface before and during the SBI. *A* and *B* correspond to an image of a single ice–water interface before the SBI (0 s) and during the SBI (52.3 s), respectively. In *A* and *B*, the interferometric fringes appear in a lateral direction. (Scale bars in *A* and *B*: 50 μm.) (*C*) A enlarged image of the region enclosed by the green rectangle in *B*. (*D*) A schematic of *C*. In this observation, $T_{\rm b}$ was changed from 3.0 °C to 2.7 °C while fixing $T_{\rm t} = -2.0$ °C.

at 0 °C (45)], λ is the wavelength of the light source (680 nm; *Materials and Methods*), and L is the interval of the fringes. From this equation, the height of the bunched step is estimated as 8×10 nm. This means that the bunched steps are composed of almost 2×10^2 elementary steps. Because $l_{\rm st} = 19.4$ μm, the elementary step spacing $l_{\rm es}$ of the initial vicinal face (before the SBI) is estimated as 9×10 nm. Thus, we obtain the tangent of the vicinal angle, $\tan\theta$ as $a/l_{\rm es} = 4 \times 10^{-3}$ (a being the height of the elementary step on the ice basal face, 0.37 nm). Furthermore, the normal growth rate of the ice interface, V, can be obtained by using the relation of $V = v_{\rm st}(h/l_{\rm st})$, the value of which is estimated as 5×10 nm/s.

Origin of SBI for Pure Melt Growth. In the following, we consider the underlying mechanism of this SBI, based on a theoretical model proposed by Chernov, Coriel, and Murray (34). This model (hereinafter the CCM model) explains that the SBI in pure melt is caused by competition among latent heat diffusion, step-advancing kinetics, and an interfacial stiffness. Hereafter, based on this model, we mainly focus on the characteristic wavelength (i.e., step spacing)—that is, the fastest-growing mode of the SBI. We note that this model does not take the degree of freedom in the direction along the step into account, which cannot explain the step defects, seen in Fig. 3*B*.

The CCM model deals with number density fluctuations of steps as step density waves. Destabilized modes of the step density waves of a growing interface are selected as a result of competition among the following three factors: 1) latent heat diffusion (the resulting temperature gradient) in the normal direction of the interface (Fig. 5*A*). The protrusions of the waves, entering lower temperature regions in the gradient, can grow faster and release latent heat. This makes the gradient of the surroundings steeper, which further accelerates the growth through facilitating heat release. This destabilizes fluctuations of all wavenumbers. 2) The Gibbs–Thomson effect, depressing the melting point due to the presence of the curvature (capillarity linked to the interfacial stiffness; Fig. 5*B*): This stabilizes larger wavenumber fluctuations. 3) A phase delay between step advancement and latent heat diffusion in the lateral direction (Fig. 5*B*): While

larger latent heat is locally generated around the bunched steps, its diffusion cannot follow the step motion—that is, the bunched steps move ahead of the heated area. The steps escaping from the heated area flow faster and then fill the valleys on the perturbed interface, which stabilize fluctuations with small wavenumbers. The fastest growing mode $q_{\rm c}$ is obtained as the wavenumber giving the positive maximum of the dispersion relation, taking the competition among the above three effects into account (*Materials and Methods*).

$$q_{\rm c} = \left(\frac{b_1}{2\,T_{\rm m}\Gamma}\right)^{1/3}. \qquad [1]$$

In this equation, the interfacial stiffness $\tilde{\gamma}$ is included in Γ as $\tilde{\gamma}/L_V$ and is the sole unknown parameter in our system (see *Materials and Methods* for the meaning and the value of each parameter). Note that $q_{\rm c} = 2\pi/l_{\rm st}$ in this system. Substituting all values in Eq. **1**, we consequently obtain $\tilde{\gamma} = 4 \times 10^{-7}$ J/m^2 for the ice basal face in the direction perpendicular to the steps.

Contrary to the other systems, for example, exhibiting q^2 to q^4 type instabilities (46), only the fluctuations around $q_{\rm c}$ are excited as the initial growth mode in this system due to the nature of the dispersion relation (34). This supports the sharp distribution of the spacing and the almost-constant step spacing of bunched steps in this system (Fig. 3 *E* and *F*). Strictly speaking, nonlinear effects of step density fluctuations also play a dominant role in the coarsening process beyond the initial stage. Nonlinear analysis
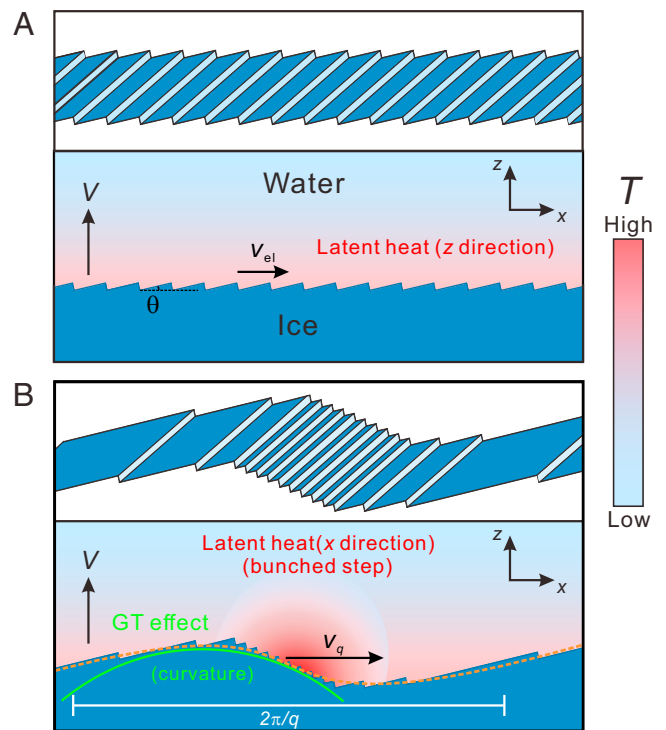

Fig. 5. Schematic representation of the mechanism of SBI. (*A*) A flat vicinal face growing with equal-spacing step propagation, whose velocity is $v_{\rm el}$ (before the SBI). A temperature gradient, resulting from latent heat generation at each step, is formed in the normal direction of the interface. (*B*) An example of a step density wave with a specific wavenumber q and a group speed v_q, formed by the SBI. A temperature gradient is formed not only in the normal (z), but also in the lateral (x), direction, resulting from the latent heat locally generated by the formation of the bunched steps. Here, the Gibbs–Thomson (GT) effect leads to the melting-point shift due to the presence of the curvature. Note also that V in *A* and *B* indicates the normal growth rate of the interface. *A* and *B*, *Upper*, show a schematic three-dimensional view.

of the CCM model is needed for understanding the behavior in more detail, which is expected to be accessible with numerical calculations.

Here, it is worth noting that, in contrast to vicinal faces, faceting crystal surfaces without any steps are stable against weak supercooling and supersaturation and do not exhibit such instabilities. Unlike the unidirectional solidification under the temperature gradient, ice crystals freely grown in supercooled water originally yield the faceting basal face. This is the reason for the gap in the observation between Ketcham and Hobbs (7) and Furukawa and colleagues (8, 9), as stated above.

Finally, we also remark on the reverse melting process. Contrary to the growth, we have observed no SBI during melting, but the interface recedes while maintaining a flat state before melting. This means that interfaces during melting are stable. This behavior is natural because the heat flow induced by melting (endothermic) suppresses interfacial fluctuations and stabilizes the interface in contrast to the case of the growth (exothermic). Therefore, for melting, all three terms in the dispersion relation (*Materials and Methods*) contribute to the stabilization of the interface.

Origin of Interactions between the Elementary Steps. The stiffness obtained above reflects the nature of interactions between elementary steps. We next examine the validity of the value obtained through a comparison to the cases of helium and silicon crystals, the best-studied substances in the area of crystal growth (Tables 1 and 2). Assuming that the step–step interaction is of the form $\phi(l) = Al^{-2}$ (A is a coefficient of the interaction strength, and the exponent corresponds to an elastic, an entropic, and an electrostatic interaction; see below), the stiffness perpendicular to the step is described as (47)

$$\tilde{\gamma} = \frac{6A}{a^3}\frac{a}{l},$$ [2]

where l is the step spacing (l being $l_{es} = 9 \times 10$ nm in this system). Substituting $\tilde{\gamma} = 4 \times 10^{-7}$ J/m² in this equation yields $A/a^3 = 2 \times 10^{-5}$ J/m². In Table 1, we summarize the surface free energy, step ledge energy, and step stiffness for ice, helium, and silicon crystals, respectively. We see that the order of each value among the three crystals almost corresponds to that of the strength of the interatomic (or intermolecular) interaction—that is, silicon (covalent bond) > ice (hydrogen bond) > helium (van der Waals bond). This one-to-one correspondence supports the validity of our estimation and the theoretical model explained above.

We further discuss the origin of the step–step interaction in this system. Here, we consider the elastic (48) and the entropic interaction (49), which are known to be the major step–step interactions with long-range repulsion, obeying $\phi(l) = Al^{-2}$. In Table 2, we summarize the values of these two interactions estimated from the theoretical calculations (*SI Appendix*) and those of helium and silicon crystals for comparison. We obtain $A_{el}/a^3 = 2.8 \times 10^{-4}$ J/m² as the elastic interaction, the value of which is one order of magnitude larger than the experimental value

Table 1. Summary of the surface free energy, step free energy, and interfacial stiffness of ice, helium, and silicon crystals

	γ (J/m²)	β/a (J/m²)	A/a^3 (J/m²)
Ice (0001)	3.3×10^{-2} [*]	9.2×10^{-3} [†]	2×10^{-5}
Helium (0001)	2.45×10^{-4} [‡]	1.1×10^{-5} [§]	4.5×10^{-5} [§]
Silicon (111)	1.2 [¶]	3.3×10^{-1} [#]	3.1×10^{-1} [#]

[*] Ref. 4.
[†] Ref. 41.
[‡] Ref. 59.
[§] Ref. 60.
[¶] Ref. 61.
[#] Ref. 62.

Table 2. Comparison of step–step interactions between experimental and theoretical estimations among ice, helium, and silicon crystals

	Elastic	Entropic	Experiment
	A_{el}/a^3 (J/m²)	A_{en}/a^3 (J/m²)	A/a^3 (J/m²)
Ice (0001)	2.8×10^{-4}	1.4×10^{-1}	2×10^{-5}
Helium (0001)	6.16×10^{-6} [*]	3.6×10^{-5} [†]	4.5×10^{-5}
Silicon (111)	1.9×10^{-2} [‡]	1.6×10^{-1} [§]	3.1×10^{-1}

[*] Ref. 59.
[†] Eq. 2 in *SI Appendix* ($T = 0.1$ K and employing the value of β/a in Table 1 [§]).
[‡] Ref. 62.
[§] Eq. 2 in *SI Appendix* ($T = 900\ °C$ [1,173 K] and employing the value of β/a in Table 1 [#]). For ice, $T = 0\ °C$ (273.15 K) is employed for the calculation of the entropic interaction. See Table 1 for the experimental values.

$A/a^3 = 2 \times 10^{-5}$ J/m². Although this mismatch may come from the rough approximation in the theoretical calculation, further careful consideration is necessary since the elastic contribution is expected to be one of the candidates for the step–step interaction in this system.

Next, we examine the entropic contribution. Note that, strictly speaking, the entropic repulsion is coupled to the elastic interaction discussed above (50). The degree of the coupling is defined as g (see *SI Appendix* for the values of each crystal). We confirm that influence of the elastic interaction is negligible in this system because of $g \ll 1$ (6.8×10^{-3} for ice). From the theoretical calculation (*SI Appendix*), we consequently obtain $A_{en}/a^3 = 1.4 \times 10^{-1}$ J/m² as the entropic interaction ($T = 0\ °C$). However, this value is ~10,000 times higher than our experimental estimation ($A/a^3 = 2 \times 10^{-5}$ J/m²). One possible explanation of this large mismatch is nonequilibrium effects on the step fluctuations. Note that the theory employed in this calculation assumes equilibrium conditions. Strictly speaking, considering the entropic repulsion during the growth (at nonequilibrium), one needs to take competition on a timescale between step-advancing dynamics and step fluctuations into account (*SI Appendix*). Thus, fluctuation modes, whose relaxation time is shorter than the characteristic time of the step-advancing dynamics, are frozen for advancing elementary steps, which diminishes the entropic repulsion through the suppression of the fluctuations. Although there have been no experimental studies on the nonequilibrium effects on the entropic interaction so far, the nonequilibrium effect is supposed to be significant in general melt growth, in the case where the step dynamics are sufficiently fast.

Our estimation may suggest the relative relevance of the elastic interaction and the possibility of the suppression of entropic interaction due to the nonequilibrium effect for ice melt growth. Here, we also remark on the possible contribution of the electrostatic (dipole–dipole) interaction. While it is basically of short range ($\propto l^{-5}$) and thus minor in comparison with the elastic and the entropic interaction, it become of long range ($\propto l^{-2}$) when the dipoles at the edge of the step tend to align in a specific direction on average (*SI Appendix*). This situation potentially realizes, taking into account the local interaction stemming from neighboring dipoles of liquid water. In a specific case (see *SI Appendix* for details), the electrostatic interaction becomes attractive, and its absolute value is the same order as that of the elastic interaction. This may imply that the net interaction is reduced and gets closer to the experimental value due to the presence of the attractive electrostatic interaction. We note that information on the orientation of dipoles at the ice–water interface would be accessible, using sum frequency generation spectroscopy. More accurate assessment of the electrostatic interaction, including elucidation of the nonequilibrium nature of the entropic interaction, is an interesting issue to be addressed in the future.

Murata et al.
Step-bunching instability of growing interfaces between ice and supercooled water

PNAS | 5 of 8
https://doi.org/10.1073/pnas.2115955119

Spiral Growth Induced by SBI. So far, we have focused on the nature of the SBI itself. Here, we reveal that the SBI triggers spiral growth via intermittent formations of screw dislocations. Fig. 6*A* shows a birth of a spiral growth during an SBI on a single ice crystal ($T_b = 2.5\,°C \rightarrow 1.7\,°C$ and $T_t = -2.0\,°C$). We find that the spiral step is induced by coalescence of unidirectional flows of bunched steps from the opposite direction (see also Movie S3). As seen in Movie S3, spiral centers initially repeat the formation and annihilation in the intermediate stage of the SBI. Then, one spiral pattern, beyond a certain size, finally overwhelms a whole ice single crystal. Here, we stress that an SBI always proceeds first, and then a spiral growth subsequently occurs, not vice versa. No screw dislocations and resulting spiral steps have been observed in the initial stage of the SBI. Thus, the screw dislocation is spontaneously induced by the SBI itself, whose Burgers vector is equal to the number of elementary steps in the step bunches. Interestingly, in Fig. 6*B* and Movie S3, we can see almost no terminations, bifurcations, and meandering of bunched steps in the spiral step, unlike the initial stage. Moreover, step spacing l_{st} keeps almost constant, even after the spiral growth overwhelms the growth (Fig. 6*C*). Here, note that the mean value of l_{st} is 17.1 μm. In general, the step spacing for spiral growth solely depends on the thermodynamic driving force. On the other hand, as discussed above, the SBI itself has a characteristic wavelength (i.e., step spacing) determined by Eq. **1**. A question here is which mechanisms are responsible for the step spacing after the appearance of the spiral mode. Ignoring strain and anisotropy of a surface, the step spacing for the spiral growth is known to be well described as (51)

$$l_{st} = \frac{19\Omega\beta}{\Delta\mu}, \qquad [3]$$

where Ω is the surface area occupied by one water molecule on the basal face (8.85×10^{-20} m^2), β is a step free energy [3.4×10^{-12} J/m (41)], and $\Delta\mu$ is the chemical potential difference between ice and water, given by $(L_m/N_A)\Delta T/T_m$, where L_m is the latent heat of ice per mole (6.01 kJ/mol), $\Delta T = T_m - T$ is the supercooling at the interface, and N_A is the Avogadro number. Here, T is an effective temperature at the interface under the temperature gradient. Also note that the expression of Eq. **3** does not depend on whether the step is elementary or bunched (see *SI Appendix* for details). Substituting all values in Eq. **3**, we obtain $\Delta T \approx 10^{-3}$ K. In contrast, the maximum supercooling at the interface (ΔT_i in Fig. 1*B*) is roughly estimated as $\Delta T \approx 10^{-1}$ K in this temperature-gradient condition ($T_b = 2.5\,°C \rightarrow 1.7\,°C$ and $T_t = -2.0\,°C$). Although an accurate value of ΔT during

the growth is unknown, the large difference in ΔT implies that Eq. **3** cannot explain the spacing of the spiral step in the SBI.

We also focus on the behavior of the late stage where the driving force approaches to zero—that is, the ice–water interface comes close to a new equilibrium position (Fig. 1*A*). If Eq. **3** mainly dominates the step spacing, l_{st} must be wider in the late stage of the process. As shown in Fig. 6*C* and Movie S3, however, the step spacing does not change, even when approaching to the new equilibrium. Thus, we can say that the step spacing is solely controlled by the SBI, not by the thermodynamics of the spiral growth.

Finally, we briefly remark on an opposite case that screw dislocations are already present on crystals before growing. In this case, the usual spiral growth initially appears and then forms the steady step trains with constant spacing, regarded as the vicinal face itself. Consequently, the SBI is also induced, even when the initial growth is driven by usual spiral growth. We emphasize that such a situation is supposed to be likely in ordinal melt growth, although direct visualizations of the spiral growth in melt have not been made so far.

Conclusions

In summary, with the aid of the optical microscopy based on the vortex retarder, we have succeeded in making in situ observations of the SBI dynamics and subsequent spiral growth in melt growth of ice crystals. Using the two-beam interferometer, we simultaneously characterized not only the step-spacing and the step-advancing velocity, but also the height of bunched steps. These quantitative observations demonstrate that the SBI in this system is explained by the vicinal face instability resulting from the competition among the latent heat diffusion, the interfacial stiffness, and the step kinetics, as predicted by Chernov et al. (34). Based on this theoretical model, we further obtain insights into the relative importance of the various mechanisms of the step–step interactions responsible for this SBI. In addition to the examination of the origin of the SBI itself, we show that the SBI induces the spiral growth via the spontaneous formation of screw dislocations by coalescence of the opposite step flows. We find that even after the ice growth is governed by the single spiral growth, the SBI is still responsible for determining the step spacing.

Although the SBI in single-component melts has been experimentally overlooked for a long time, its mechanism is general for ordinal melt growth. So, by tuning the normal growth rate, e.g., by the temperature-gradient system employed in this study, this type of SBI is expected to be observed in a wide variety of substances, ranging from molecular crystals to semiconductors
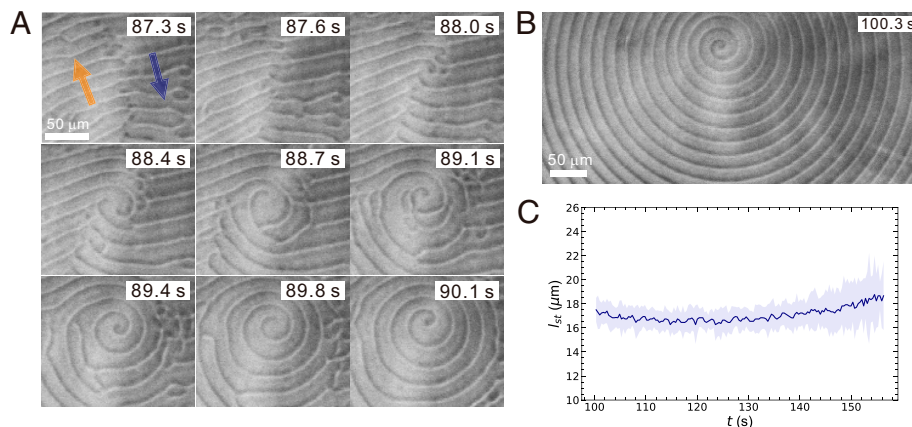

Fig. 6. A birth of a spiral growth induced by the SBI. (*A*) Sequential images of the birth process of the spiral growth mode. Here, T_b was changed from 2.5 °C to 1.7 °C while fixing $T_t = -2.0$ °C. The orange and blue arrows at 87.3 s show the flow directions of bunched steps. (*B*) An image after the formation of the spiral growth mode. (Scale bars: 50 μm.) (*C*) A temporal change of the step spacing, l_{st}, after the spiral formation.

and metals. For example, such moderate growth conditions can be achieved in the so-called zone-refining process, a well-known method for purifying crystalline materials (see Chapter 5 in ref. 52). Moreover, the SBI may play a crucial role in the production process of bulk single crystals because its growth condition is usually shallow supercooling. So, our findings offer insights into the fundamental understanding for making high-quality and high-performance crystals, which is significant in industrial and material sciences.

Furthermore, this study, together with our previous one (41), reveals the presence of the elementary step on the genuine ice basal face, contrary to the conventional wisdom that regards crystal–melt (solid–liquid) interfaces as basically diffuse at the molecular level. Thus, direct visualizations of the elementary step on the genuine ice basal face, freely growing in supercooled water, may be achieved by improving the height sensitivity and time resolution of our optical system, which is an experimental challenge to be addressed in the future. In addition, our experimental system is expected to serve as a model for studying pinning effects on elementary and bunched steps by an impurity adsorbed on the crystal surface. For ice crystals, it is known that such effects are brought by a bio-macromolecule—for example, antifreeze proteins (AFP) (53)—and results in inhibition of ice-crystal growth (54–56), which is closely related to cryoprotection and cryopreservation of biological materials, such as cells, tissues, and organs. In this context, elucidating dynamic interactions between advancing steps and AFP is significant, which remains a potential area for future research.

Materials and Methods

Optical Microscopy System. Our advanced optical microscopy is composed of a confocal scanning unit (FV300; Olympus Optical Co. Ltd.) attached to an inverted optical microscope (IX70; Olympus Optical Co. Ltd.). As a light source of the microscopy, a superluminescent diode (SLD; ASLD68-050-B-FA, 680 nm; Amonics Ltd.) was used to avoid appearance of unnecessary interference fringes and speckles, lowering the quality of images. The coherent length and full-width at half-maximum of this SLD were about 10 μm and 5 nm, respectively. In this study, unlike the conventional LCM-DIM, we used a vortex retarder (the vortex order, $m = 1$, was a special order for 680-nm light source; Thorlabs, Inc.) instead of a Nomarski prism (see *SI Appendix* for details). For interferometric observations, instead of a usual objective (UPlanFL N, 10x/0.3, Olympus Optical Co. Ltd.), we used a Michelson-type objective (CF Plan, 5x/0.13, Nikon Co. Ltd.; a special order), having an adjustable reference mirror. This adjusting mechanism is necessary for interferometric observations to optimize the optical pass length corresponding to the thickness of the supercooled water in the observation chamber. The interferometric observations were performed by combining the Michelson-type objective with the optical microscopy.

Samples. In this study, ultrapure water (>18.2 MΩ·cm) was used for observations of ice-melt growth. To check the height resolution of the optical microscopy, we employed a gypsum (010) surface as a standard sample. The molecular height steps were prepared by cleaving a bulk gypsum crystal. The height profile and the differential images of the gypsum (010) surface (*SI Appendix*, Fig. S2) were obtained by AFM (Veeco Dimension 3100 AFM).

Observation Chamber. The observation chamber was composed of upper and lower Cu plates, whose temperatures were separately controlled by using Peltier elements in order to produce a temperature gradient crossing the ice-melting point. We set the upper plate as the lower-temperature side (ice) and the lower plate as the higher-temperature side (water), taking the density difference between ice and water and the observations with an inverted microscope into account. The gap between the upper and the lower plates was set as 2 mm. The temperature gradient of the system arises along the light axis of the microscope, and the observation plane corresponds to the vicinal basal face of ice crystals at the ice melting point. We controlled the top and the bottom temperatures at the level of 0.1 °C, of which fluctuation is within 0.01 °C. We also note that, instead of usual cover glasses, CaF_2 was used as a window of the observation chamber (Fig. 1A) to reduce the reflection from the window in the observation plane and improve the heat conduction from the top and bottom plates. CaF_2 has an ∼10 times higher thermal conductivity than the usual cover glass.

Dispersion Relation of SBI. Within the linear stability analysis, the growth rate of the amplitude of step density waves, σ, is described as the following dispersion relation (34, 35).

$$\sigma \sim (K_{st}\bar{p}) \left[\frac{V(L_V/\bar{c})}{2\bar{\kappa}} - T_m\Gamma q^2 - \frac{b_1}{q} \right], \qquad [4]$$

where q is the wavenumber of the step density waves, V is the normal growth rate of the crystal–melt interface (5×10 nm/s in this system), K_{st} is the step kinetic coefficient, T_m is the melting point of ice (273.15 K), $\bar{p}$ is the tangent of the vicinal face ($\tan\theta = 4 \times 10^{-3}$; see *Spatiotemporal Dynamics of SBI*), L_V is the latent heat of ice per unit volume (3.06×10^8 J/m^3), $\Gamma = \tilde{\gamma}/L_V$ is the capillary length, and $\tilde{\gamma}$ is the interfacial stiffness. In addition, $\bar{c}$ is the effective heat capacity at the interface, written as $k_s/(2\kappa_s) + k_l/(2\kappa_l)$, where k_s and k_l are the thermal conductivities of ice [1.59 W/m· K (57)] and water [0.560 W/m· K (58)], κ_s and κ_l are the thermal diffusivities of ice [8.43×10^{-7} m^2 /s (57)] and water [1.35×10^{-7} m^2 /s (57)], respectively. Here, $\bar{\kappa}$ is the effective thermal conductivity at the interface (3.56×10^{-7} m^2 /s), written as $\bar{k}/\bar{c}$, where $\bar{k} = (k_s + k_l)/2$ (the effective thermal conductivity at the interface). Note that $b_1 = [V^2(L_V/\bar{c})]/[(2\bar{\kappa}\bar{p})^2]$. In Eq. 4, for $\sigma < 0$, a stepped interface is stable against the fluctuations, whereas for $\sigma > 0$, it is unstable. We note that the first, second, and third terms in Eq. 4 correspond to the effects of 1), 2), and 3), respectively (see *Origin of SBI for Pure Melt Growth*).

Data Availability. All study data are included in the article and/or supporting information.

1. T. Bartels-Rausch *et al.*, Ice structures, patterns, and processes: A view across the icefields. *Rev. Mod. Phys.* **84**, 885–944 (2012).
2. J. S. Wettlaufer, J. G. Dash, N. Untersteiner, Eds., *Ice Physics and the Natural Environment* (NATO ASI Series, Springer, Berlin, 1999).
3. H. Pruppacher, J. Klett, *Microphysics of Clouds and Precipitation* (Atmospheric and Oceanographic Sciences Library, Springer, Dordrecht, Netherlands, ed. 2, 1978).
4. P. V. Hobbs, *Ice Physics* (Oxford University Press, New York, 1974).
5. J. S. Langer, Instabilities and pattern formation in crystal growth. *Rev. Mod. Phys.* **52**, 1–28 (1980).
6. A. Chernov, *Modern Crystallography III* (Springer Series in Solid-State Sciences, Springer, Berlin, ed. 1, 1984), vol. 36.
7. W. M. Ketcham, P. V. Hobbs, Step growth on ice during the freezing of pure water. *Philos. Mag.* **18**, 659–661 (1968).
8. S. Adachi *et al.*, Stable growth mechanisms of ice disk crystals in heavy water. *Phys. Rev. E Stat. Nonlin. Soft Matter Phys.* **84**, 051605 (2011).
9. E. Yokoyama *et al.*, Measurements of growth rates of an ice crystal from supercooled heavy water under microgravity conditions: Basal face growth rate and tip velocity of a dendrite. *J. Phys. Chem. B* **115**, 8739–8745 (2011).
10. N. Ohtani, M. Katsuno, J. Takahashi, H. Yashiro, M. Kanaya, Evolution of macrosteps on $6H - SiC(0001)$: Impurity-induced morphological instability of step trains. *Phys. Rev. B* **59**, 4592–4595 (1999).
11. C. Schelling, G. Springholz, F. Schäffler, Kinetic growth instabilities on vicinal Si(001) surfaces. *Phys. Rev. Lett.* **83**, 995–998 (1999).
12. Y. Homma, N. Aizawa, Electric-current-induced step bunching on Si(111). *Phys. Rev. B* **62**, 8323–8329 (2000).
13. C. Schelling, M. Mühlberger, G. Springholz, F. Schäffler, $Si_{1-x}Ge_x$ growth instabilities on vicinal si(001) substrates: Kinetic vs. strain-induced effects. *Phys. Rev. B* **64**, 041301 (2001).
14. K. Yagi, H. Minoda, M. Degawa, Step bunching, step wandering and faceting: Self-organization at Si surfaces. *Surf. Sci. Rep.* **43**, 45–126 (2001).
15. J. Bao, O. Yasui, W. Norimatsu, K. Matsuda, M. Kusunoki, Sequential control of step-bunching during graphene growth on SiC (0001). *Appl. Phys. Lett.* **109**, 081602 (2016).
16. P. Tejedor, P. Šmilauer, C. Roberts, B. A. Joyce, Surface-morphology evolution during unstable homoepitaxial growth of GaAs(110). *Phys. Rev. B* **59**, 2341–2345 (1999).
17. P. G. Vekilov, Y. G. Kuznetsov, A. A. Chernov, The effect of temperature on step motion; (101) ADP face. *J. Cryst. Growth* **121**, 44–52 (1992).
18. T. A. Land, T. L. Martin, S. Potapenko, G. T. Palmore, J. J. De Yoreo, Recovery of surfaces from impurity poisoning during crystal growth. *Nature* **399**, 442–445 (1999).
19. N. A. Booth, A. A. Chernov, P. G. Vekilov, Characteristic lengthscales of step bunching in KDP crystal growth: In situ differential phase-shifting interferometry study. *J. Cryst. Growth* **237-239**, 1818–1824 (2002).

Murata et al.
Step-bunching instability of growing interfaces between ice and supercooled water

PNAS | 7 of 8
https://doi.org/10.1073/pnas.2115955119

20. J. Bisschop, D. K. Dysthe, Instabilities and coarsening of stressed crystal surfaces in aqueous solution. *Phys. Rev. Lett.* **96**, 146103 (2006).

21. M. Maruyama *et al.*, Effects of a forced solution flow on the step advancement on 110 faces of tetragonal lysozyme crystals: Direct visualization of individual steps under a forced solution flow. *Cryst. Growth Des.* **12**, 2856–2863 (2012).

22. R. L. Schwoebel, E. J. Shipsey, Step motion on crystal surfaces. *J. Appl. Phys.* **37**, 3682–3686 (1966).

23. V. I. Marchenko, A. Y. Parshin, Elastic properties of crystal surfaces. *Sov. Phys. JETP* **52**, 129–131 (1980).

24. J. Tersoff, Y. H. Phang, Z. Zhang, M. G. Lagally, Step-bunching instability of vicinal surfaces under stress. *Phys. Rev. Lett.* **75**, 2730–2733 (1995).

25. D. Kandel, J. D. Weeks, Simultaneous bunching and debunching of surface steps: Theory and relation to experiments. *Phys. Rev. Lett.* **74**, 3632–3635 (1995).

26. Y. N. Yang, E. S. Fu, E. D. Williams, An STM study of current-induced step bunching on Si(111). *Surf. Sci.* **356**, 101–111 (1996).

27. M. Sato, M. Uwaha, Growth of step bunches formed by the drift of adatoms. *Surf. Sci.* **442**, 318–328 (1999).

28. O. Toktarbaiuly *et al.*, Step bunching with both directions of the current: Vicinal W(110) surfaces versus atomistic-scale model. *Phys. Rev. B* **97**, 035436 (2018).

29. C. Zhu *et al.*, Influence of solution flow on step bunching in solution growth of SiC crystals. *Cryst. Growth Des.* **13**, 3691–3696 (2013).

30. K. Ariyawong, Y. J. Shin, J.-M. Dedulle, D. Chaussende, Analysis of macrostep formation during top seeded solution growth of $4H - SiC$. *Cryst. Growth Des.* **16**, 3231–3236 (2016).

31. D. Kandel, J. D. Weeks, Theory of impurity-induced step bunching. *Phys. Rev. B Condens. Matter* **49**, 5554–5564 (1994).

32. H. Müller-Krumbhaar, J. P. v d Eerden, Dynamic coarsening of crystal surfaces by formation of macrosteps. *Phys. Rev. Lett.* **57**, 2431–2433 (1986).

33. J. F. Lutsko, A. E. S. Van Driessche, M. A. Durán-Olivencia, D. Maes, M. Sleutel, Step crowding effects dampen the stochasticity of crystal growth kinetics. *Phys. Rev. Lett.* **116**, 015501 (2016).

34. A. A. Chernov, S. R. Coriell, B. T. Murray, Kinetic self-stabilization of a stepped interface: Growth into a supercooled melt. *J. Cryst. Growth* **149**, 120–130 (1995).

35. S. R. Coriell, B. T. Murray, A. A. Chernov, Kinetic self-stabilization of a stepped interface: Binary alloy solidification. *J. Cryst. Growth* **141**, 219–233 (1994).

36. G. J. Morris, E. Acton, Controlled ice nucleation in cryopreservation—A review. *Cryobiology* **66**, 85–92 (2013).

37. G. Sazaki *et al.*, In situ observation of elementary growth steps on the surface of protein crystals by laser confocal microscopy. *J. Cryst. Growth* **262**, 536–542 (2004).

38. G. Sazaki, S. Zepeda, S. Nakatsubo, E. Yokoyama, Y. Furukawa, Elementary steps at the surface of ice crystals visualized by advanced optical microscopy. *Proc. Natl. Acad. Sci. U.S.A.* **107**, 19702–19707 (2010).

39. G. Sazaki, S. Zepeda, S. Nakatsubo, M. Yokomine, Y. Furukawa, Quasi-liquid layers on ice crystal surfaces are made up of two different phases. *Proc. Natl. Acad. Sci. U.S.A.* **109**, 1052–1055 (2012).

40. K. I. Murata, H. Asakawa, K. Nagashima, Y. Furukawa, G. Sazaki, Thermodynamic origin of surface melting on ice crystals. *Proc. Natl. Acad. Sci. U.S.A.* **113**, E6741–E6748 (2016).

41. K. I. Murata, K. Nagashima, G. Sazaki, How do ice crystals grow inside quasiliquid layers? *Phys. Rev. Lett.* **122**, 026102 (2019).

42. G. Sazaki, K. Nagashima, K.-i. Murata, Y. Furukawa, In-situ observation of crystal surfaces by optical microscopy. *Prog. Cryst. Growth Charact. Mater.* **62**, 408–412 (2016).

43. H.-C. Jeong, E. D. Williams, Steps on surfaces: Experiment and theory. *Surf. Sci. Rep.* **34**, 171–294 (1999).

44. A. V. Latyshev, A. L. Aseev, A. B. Krasilnikov, S. I. Stenin, Transformations on clean Si(111) stepped surface during sublimation. *Surf. Sci.* **213**, 157–169 (1989).

45. H. Eisenberg, Equation for the refractive index of water. *J. Chem. Phys.* **43**, 3887–3892 (1965).

46. M. Sato, M. Uwaha, Morphological instability caused by asymmetry in step kinetics. *Phys. Rev. B Condens. Matter* **51**, 11172–11175 (1995).

47. P. Nozières, "Shape and growth of crystals" in *Solids Far from Equilibrium*, C. Godreche, Ed. (Collection Alea-Saclay: Monographs and Texts in Statistical Physics, Cambridge University Press, Cambridge, UK, 1992), pp. 1–154.

48. A. Pimpinelli, J. Villain, *Physics of Crystal Growth* (Cambridge University Press, Cambridge, UK, 1998).

49. Y. Akutsu, N. Akutsu, T. Yamamoto, Universal jump of Gaussian curvature at the facet edge of a crystal. *Phys. Rev. Lett.* **61**, 424–427 (1988).

50. T. Yamamoto, Y. Akutsu, N. Akutsu, Fluctuation of a single step on the vicinal surface-universal and non-universal behaviors. *J. Phys. Soc. Jpn.* **63**, 915–925 (1994).

51. N. Cabrera, M. M. Levine, XLV. On the dislocation theory of evaporation of crystals. *Philos. Mag.* **1**, 450–458 (1956).

52. M. E. Glicksman, *Principles of Solidification: An Introduction to Modern Casting and Crystal Growth Concepts* (Springer, New York, ed. 1, 2011).

53. Y. Yeh, R. E. Feeney, Antifreeze proteins: Structures and mechanisms of function. *Chem. Rev.* **96**, 601–618 (1996).

54. Y. Furukawa *et al.*, Crystal-plane-dependent effects of antifreeze glycoprotein impurity for ice growth dynamics. *Philos. Trans.- R. Soc., Math. Phys. Eng. Sci.* **377**, 20180393 (2019).

55. Y. Furukawa *et al.*, Oscillations and accelerations of ice crystal growth rates in microgravity in presence of antifreeze glycoprotein impurity in supercooled water. *Sci. Rep.* **7**, 43157 (2017).

56. S. Zepeda, E. Yokoyama, Y. Uda, C. Katagiri, Y. Furukawa, In situ observation of antifreeze glycoprotein kinetics at the ice interface reveals a two-step reversible adsorption mechanism. *Cryst. Growth Des.* **8**, 3666–3672 (2008).

57. D. W. James, The thermal diffusivity of ice and water between -40 and $+60$ °C. *J. Mater. Sci.* **3**, 540–543 (1968).

58. M. L. V. Ramires *et al.*, Standard reference data for the thermal conductivity of water. *J. Phys. Chem. Ref. Data* **24**, 1377–1381 (1995).

59. S. Balibar, H. Alles, A. Y. Parshin, The surface of helium crystals. *Rev. Mod. Phys.* **77**, 317–370 (2005).

60. E. Rolley, E. Chevalier, C. Guthmann, S. Balibar, Stepped surfaces of hcp helium-4 crystals. *Phys. Rev. Lett.* **72**, 872–875 (1994).

61. R. Tran *et al.*, Surface energies of elemental crystals. *Sci. Data* **3**, 160080 (2016).

62. C. Alfonso, J. M. Bermond, J. C. Heyraud, J. J. Métois, The meandering of steps and the terrace width distribution on clean Si(111): An in-situ experiment using reflection electron microscopy. *Surf. Sci.* **262**, 371–381 (1992).